



City Research Online

City, University of London Institutional Repository

Citation: Abdulsalam, M., Ahiska, K. & Aouf, N. A novel UAV-integrated deep network detection and relative position estimation approach for weeds. Proceedings of the Institution of Mechanical Engineers, Part G: Journal of Aerospace Engineering, 237(10), pp. 2211-2227. doi: 10.1177/09544100221150284

This is the published version of the paper.

This version of the publication may differ from the final published version.

Permanent repository link: <https://openaccess.city.ac.uk/id/eprint/29996/>

Link to published version: <https://doi.org/10.1177/09544100221150284>

Copyright: City Research Online aims to make research outputs of City, University of London available to a wider audience. Copyright and Moral Rights remain with the author(s) and/or copyright holders. URLs from City Research Online may be freely distributed and linked to.

Reuse: Copies of full items can be used for personal research or study, educational, or not-for-profit purposes without prior permission or charge. Provided that the authors, title and full bibliographic details are credited, a hyperlink and/or URL is given for the original metadata page and the content is not changed in any way.

City Research Online:

<http://openaccess.city.ac.uk/>

publications@city.ac.uk

A novel UAV-integrated deep network detection and relative position estimation approach for weeds

Mahmoud Abdulsalam¹ , Kenan Ahiska²  and Nabil Aouf¹

Proc IMechE Part G:
J Aerospace Engineering
2023, Vol. 0(0) 1–17
© IMechE 2023



Article reuse guidelines:

sagepub.com/journals-permissions
DOI: 10.1177/09544100221150284
journals.sagepub.com/home/pig



Abstract

This paper aims at presenting a novel monocular vision-based approach for drones to detect multiple type of weeds and estimate their positions autonomously for precision agriculture applications. The methodology is based on classifying and detecting the weeds using a proposed deep neural network architecture, named fused-YOLO on the images acquired from a monocular camera mounted on the unmanned aerial vehicle (UAV) following a predefined elliptical trajectory. The detection/classification is complemented by a new estimation scheme adopting unscented Kalman filter (UKF) to estimate the exact location of the weeds. Bounding boxes are assigned to the detected targets (weeds) such that the centre pixels of the bounding box will represent the centre of the target. The centre pixels are extracted and converted into world coordinates forming azimuth and elevation angles from the target to the UAV, and the proposed estimation scheme is used to extract the positions of the weeds. Experiments were conducted both indoor and outdoor to validate this integrated detection/classification/estimation approach. The errors in terms of misclassification and mispositioning of the weeds estimation were minimum, and the convergence of the position estimation results was short taking into account the affordable platform with cheap sensors used in the experiments.

Keywords

deep neural networks, artificial intelligence, position estimation, robotic vision, weed detection, precision agriculture, unmanned aerial vehicles

Date received: 9 November 2021; accepted: 15 December 2022

Introduction

Agriculture as a whole provides a means of livelihood ranging from food production, pharmaceuticals, textiles and raw materials for industries. However, the productivity of this sector is threatened by the existence of weeds which are parasitic in nature.¹ Weeds are unwanted plants that grow on the farmland and compete with the desired plants for water, nutrients, space and sunlight. The losses in productivity reach 25% in Europe, but in the less developed areas in Africa and Asia, almost half of the potential food yield is lost due to weeds.² It is reported that lettuce yield is reduced over 50% due to weeds,³ wheat yield is reduced by 15%⁴ and there is up to 71% drop in seeded tomato yield⁵ due to weed infestation.

Conventionally, weeds are removed using crude tools and herbicides. However, these processes are wasteful and dangerous to the environment since these herbicides are made of harmful chemicals. To efficiently remove weeds, there is a need to carefully identify the weed, then localize its exact position and then finally apply the right quantity of the herbicides or deploy the appropriate tool for the weed removal. This gives rise to the consideration of

robotics platforms for weed removal. While some works have proposed mechanical robotic tools,^{1,6} others proposed robotic sprayers to reach the objective.^{7–10}

Weeds can be identified using computer vision techniques.^{1,11} The adoption of deep neural networks (DNNs) for weed detection is increasing.^{12–14} To bridge the gap between weed detection and precise weed removal, this paper addresses the problem of identification and localization of the weeds.

Commercially available systems for smart weed detection and removal are generally expensive. The availability of affordable off-the-shelf unmanned aerial vehicles (UAVs) with essential sensors makes it pertinent

¹Electrical / Electronic Engineering, City University of London, London, UK

²Defence Systems Technologies Department, Aselsan Inc. Turkey, Ankara, Turkey

Corresponding author:

Mahmoud Abdulsalam, Electrical / Electronic Engineering, City University of London, Northampton Square, London EC1V 0HB, UK.
Email: mahmoud.abdulsalam@city.ac.uk

to exploit them for this research. The fusion of the information from several sensors through a robotics operating system (ROS)¹⁵ makes it possible to perform several complicated tasks through effective communication between the sensors. Works such as navigation,¹⁶ path planning¹⁷ and localization of targets¹⁸ have been possible through this set-up. Thus, we seek to exploit an affordable platform for this work and extend the solution scope to localizing and estimating the relative position of the weed.

In this paper, a Parrot AR drone platform is subjected to a predefined elliptic trajectory, and the stream of images from a monocular camera mounted on it are acquired throughout its motion. The stream of images are utilized to precisely detect the object of interest in the images using a deep detection network. The used network is a cascaded ResNet-50¹⁹ and YOLOv4.²⁰ The detected weeds are then assigned to bounding boxes, and the centre pixels of the assigned bounding boxes are extracted. A centre pixel is assumed to be the centre of the detected weed, and it is transformed from image frame to world coordinates. Azimuth and elevation angles of the target centre point with respect to the are extracted and later fused in the unscented Kalman filter (UKF)²¹ to estimate the location of the weed. The contributions of the paper are twofold: (1) utilizing an affordable platform equipped with a monocular camera for accurate multiple target position estimation and (2) extending the use of a DNN output beyond detection and identification to relative position estimation such that the information obtained from the detection network (bounding boxes, region of interest pixels) can be further processed to achieve relative position estimation of the detected target.

The paper continues with a literature review in the next section. The simulation and experimental frameworks are discussed in the subsequent sections. The results are demonstrated and discussed in the final sections.

Literature review

Weed detection using feature extraction in image processing is the earliest technique used to identify weeds with computer vision. Edge detection has been utilized as a technique for weed detection.^{22,23} However, the main plant and weed cannot be effectively differentiated using edge detection only. Different illumination conditions can be used to improve the detection using a colour model and split component of gray images.⁷ A vertical projection method and a linear scanning method are combined to quickly identify the centre line of the crop rows. However, in this method, it is assumed that every plant detected outside the centre line of the crop rows is a weed. This is not always the case as weeds can also grow along the centre line. Machine learning techniques provided results that perform better if weeds are not on the centre line of the crop rows.^{13,24} Nevertheless, all these methods are not capable of precisely detecting the exact specie of weed. These limitations prompted the use of DNN for weed detection.

Weed detection was performed for perennial rye-grass with deep learning convolutional neural network.¹⁴ The work concluded that VGGNet²⁵ performed better with the rye-grass dataset. This performance can be improved by capturing sequential information and combining RGB and NIR images.²⁶ The drawback to this work is again the lack of weed specie detection for accurate herbicide selection. Another work investigated the combination of classification and detection for fruits.¹² Similarly, in our previous work, we combined a classification and detection network for weed detection.²⁷ This way, we can categorically tell the type of weed and identify a region of interest (ROI) for further processing.

The accuracy of weed detection can be impacted by many factors such as variable lighting condition, sun angles, occluded and damaged plant leaves, and changing morphological or spectral properties of plant leaves at different growth stages.²⁸ It becomes imperative to use a rich dataset for training with different conditions. The conventional four steps in the procedure for using ground-based machine vision and imaging processing techniques in weed detection are the pre-processing, segmentation, feature extraction and classification.²⁹ We aim at extending this procedure to localizing and estimating the relative position of the weed.

The crowded literature on target localization can be grouped according to the platform used,^{30,31} or the sensors employed^{18,32} or the estimation model studied.^{31,33} The main aim for all is to maximize the localization accuracy and minimize the time required. Few however seek to use small UAVs with affordable sensors to achieve a high performance. A combination of 2D laser range finder with a monocular camera can be used for the localization.³⁰ Although the maximum deviation recorded using this method was about 13% from the actual measurement. This may be due to the not so robust target detection process employed in the paper. Edge detection and colour detection were utilized to detect the only green circular target in the scene. In reality, there can be many targets with seemingly similar features. Moreover, using this approach to detect the target while in flight can cause target blurring. An alternative approach was presented based on real-time kinematic positioning and thermal imagery.³³ This approach is based on the assumption that as long as a ground rover and a base station maintain at least 5 satellites in common, there can be an accurate prediction of the rover's location.

The first to exploit the combination of UAV state estimates with the image data to acquire bearing measurements of the target and utilizing them in the target localization is Ponda et al.³⁴ In their work, a fixed wing UAV was subjected to numerous trajectories to find the optimal trajectory for target localization. The image data of the target are processed to obtain bearing angles from the drone to the target, and an extended Kalman filter (EKF) is used for position estimation. Even though it is a simulation work, good estimation results were obtained after 50 measurements for a single target. Another work also attempted the estimation with a fixed wing UAV and

using a recursive least squares (RLS) filter but suffered a wide error of 10.9 m.³¹ To tackle the limitations of fixed wing UAV particularly in manoeuvrability and altitude of flight, a quad-rotor can be used.³¹ Accurate results were obtained after 30 seconds for a single target using this method.

Methodology

Problem definition

The problem is to estimate the exact position of the weed using a UAV with no sophisticated sensors. An affordable platform equipped with monocular camera with no sufficient information such as depth being generated makes it difficult to estimate the positions of weeds relative to the platform. The idea is to utilize the camera to detect a target and utilize the detection bounding boxes to estimate the target's position. To do so, first the platform identifies/detects and localizes the target in the image frame. We used our trained network for the target detection and performed some post-processing to localize the target in the image frame. Second, the information from bounding boxes are used to estimate the centre position in the image frame. Since the objective is to reach a solution with a monocular camera set-up, where the depth information is not readily at hand as in the case of a stereo camera set-up, we converted the bounding box's centre pixels to bearing angles and afterwards into azimuth and elevation angles (further explained in the Technical and Theoretical Approach section) with respect to the UAV. Thus, our problem can be divided into (1) acquiring the images from a monocular camera and transferring them to the ground station together with the position of the UAV, (2) detection and classification of the weed from a monocular camera, (3) extracting the position of the weed in the image frame and (4) estimating the position of the weed in the world frame. In order to have an accurate estimate for world coordinates of the weed, measurements regarding this information should be rich. The UAV is controlled to make a predefined ellipse trajectory. The nature of the trajectory is an important factor of the estimation accuracy as the field of view (FOV) varies from one point to another along the trajectory. Since the targets are at a stationary position, we try to limit the FOV of the camera to cover all the targets at each point along the trajectory so that we can obtain updates from each target simultaneously. A constant trajectory altitude at 1 m is selected. The bearing angle measurements for the position of the weed are fused in a UKF framework.

Technical and theoretical approach

The solution approach is summarized in a process flow chart shown in Figure 1. The process flow encompasses mainly the data acquisition section, and the ROS nodes on the ground station and the output section. The input data acquisition section is the hardware that provides inputs to the system. The image stream from the monocular camera

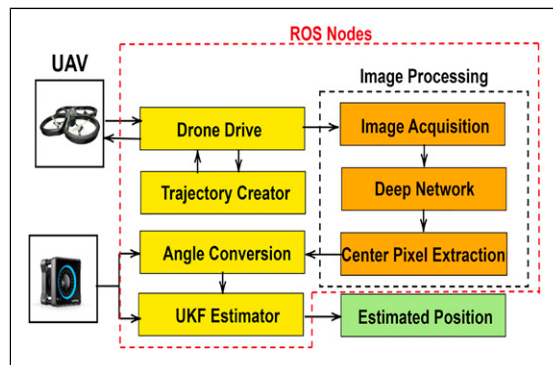


Figure 1. Solution architecture.

mounted on the drone, and the ground truth positions of the UAV and the target (weed) measured by the tracking system are the inputs to the process. The ROS nodes hosted on a ground station with core-i7 processing power are the main processing part of the system. Detection and classification of the weed using a DNN, centre pixel extraction on the images, calculating the bearing angles, fusing the bearing angles to estimate world coordinates of the weed with UKF and the trajectory planning with drone driving tasks are performed on the ROS nodes. The output section consists of position coordinates of the estimated target (weed).

Unmanned aerial vehicle and tracking system. The UAV used is an affordable off-the-shelf Parrot AR drone. It is a six degree-of-freedom quadcopter with a miniaturized IMU, an ultrasonic sensor, a frontal camera with 720p sensor and 93° lens, a downward/vertical camera with QVGA sensor with 64° lens and 4 brushless 14.5 watt, 28.500 RPM in-runner type motors.³⁵ The tracking system is a set of cameras with 1.3 MP resolution, ± 0.30 mm 3D accuracy, 240 frames per second (FPS) native frame rate and 1000 FPS max frame rate which are used for tracking.³⁶

Drone driver. The drone driver is a ROS package that consists of all the libraries of the Parrot drone's sensors and inbuilt controllers. We utilize the drone driver to control the drone and also to receive image feeds from the drone's camera. The planar velocity references in UAV frame $V_x^{(u)}$ and $V_y^{(u)}$ indicated with the superscript u are transferred from the reference position derivatives defined in ground frame indicated with the superscript g , namely, $\dot{X}_d^{(g)}$ and $\dot{Y}_d^{(g)}$ in this drone driver ROS node as well

$$\left(V_x^{(u)}(t), V_y^{(u)}(t) \right) = T_g^u \left(\dot{X}_d^{(g)}(t), \dot{Y}_d^{(g)}(t) \right) \quad (1)$$

where T_g^u is the reference frame transformation from ground frame to world frame.

Trajectory creator. This node provides the profile of trajectory to be performed by the drone and updates the drone driver with the necessary control parameters for following

this trajectory. In this work, an ellipse trajectory is employed taking inspiration from the circular proposed for target localization.⁸ We modified this to an ellipse so that the neighbouring targets can fit into the FOV. The trajectory profile is defined as follows

$$\begin{aligned} X_d^{(g)}(t) &= a \cos(\omega t) \\ Y_d^{(g)}(t) &= b \sin(\omega t) \end{aligned} \quad (2)$$

Therefore

$$\begin{aligned} \dot{X}_d^{(g)}(t) &= -a\omega \sin(\omega t) \\ \dot{Y}_d^{(g)}(t) &= b\omega \cos(\omega t) \end{aligned} \quad (3)$$

where a and b are radii in x and y axis, respectively. ω is the angular velocity, and t is the time.

Image acquisition. This node receives image data from the drone driver and distributes to the detection network via an image transport link. Images are transported in the form of messages at a frequency of 200 Hz so they can effectively be utilized by the detection network. The drone's camera was calibrated beforehand and the parameters were obtained.

Deep network. Conventionally, approaches such as colour detection or edge detection are deployed for weed detection problem.^{18,37} Most of the time, weeds have about 90% resemblance with the main plant. To contain this, a DNN is used to detect the weeds, similar to our previous work²⁷ but with modifications to suit this peculiar problem. The network is a cascade of a classification network ResNet-50 and a detection network YOLOv4. A detection network is necessary since using a classification network alone will classify the entire image as a weed which includes the ROI and the background without categorically indicating the weed within the image. In this paper, it is required to know the region within the image that corresponds to the weed. The choice of ResNet-50 as the classification network is pertinent to the work of the accuracy obtained in fruit classification.¹² YOLO framework was selected since the speed of detection for this network is almost twice as fast as two-staged detectors in weed detection.²⁷ This architecture is 95%–98% effective in weed classification and detection.²⁷ The network was

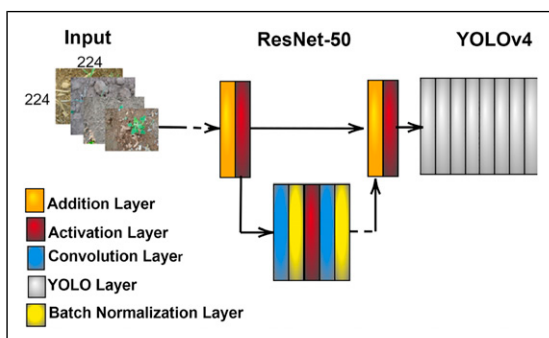


Figure 2. Fused-YOLO deep neural network architecture.

trained with a dataset of 2000 images of the weed obtained from form.³⁸

The DNN used for this work is shown in Figure 2. The final layers of the ResNet-50, namely, average pooling layer, fully connected layer, softmax and classification layers were truncated and merged with a YOLOv4 network. The final activation layer of the ResNet-50 was utilized as the feature extraction layer of the YOLOv4 so that the activation layer becomes the input to the YOLOv4. In the rest of the paper, this architecture will be referred as fused-YOLO.

The input layers of the trained network are not compatible with the output coming from the drone camera. An encoding–decoding operation was performed as shown in Figure 3 to remap and rearrange the pixels.

The encoding–decoding process was done to rearrange all the pixels from the drone camera to fit into the input layer of the fused-YOLO. The fused-YOLO receives images from the image acquisition node as input, the targets/weeds are detected and a bounding box is assigned for each weed detected as seen in Figure 4.

Centre pixel extraction. After each detection, the centre pixel of the detection bounding box is extracted. It is assumed that the centre of the bounding box coincides with the centre of the weed whose position is to be estimated as in Figure 4. This location in the image frame is converted to world coordinates as the geometric centre of the weed

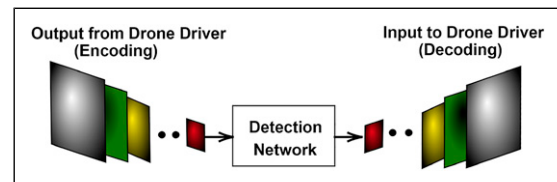


Figure 3. Encoding–decoding of images.

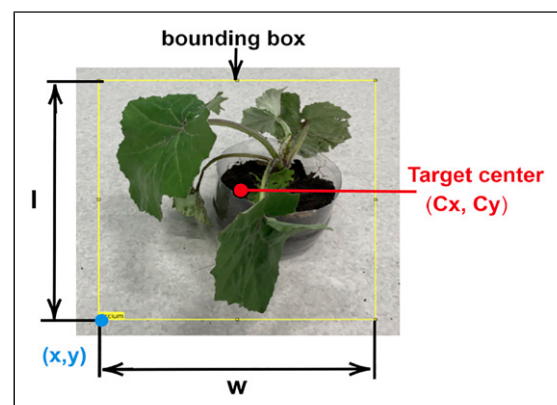


Figure 4. Bounding box extraction. l and w are the length and width of the bounding box, respectively. (x, y) represents the origin of the bounding box. (C_x, C_y) represents the target centre.

$$\begin{aligned} C_x &= x_p + \frac{w}{2} \\ C_y &= y_p + \frac{l}{2} \end{aligned} \quad (4)$$

where C_x and C_y are the centre pixel coordinates, x_p and y_p are the origin points of the bounding box, and l and w are the length and width of the bounding box. All the variables are updated with each detection made.

Calculation of bearing angles. Provided the frontal camera orientation and pointing axis are known, using the Parrot drone on-board inertial measurement unit (IMU) and the odometry information, the centre pixels are converted to bearing angles ($\alpha_1, \alpha_2, \beta_1, \beta_2, \dots$) from the camera pointing axis to a vector that passes through the targets and the focal point¹⁸ as shown in Figure 5. Afterwards, these angles are converted into the overall azimuth and elevation angles (σ_1 and θ_1, σ_2 and θ_2, \dots) for each target as depicted in Figure 6 through a sequence of conversions (camera frame to drone's body frame and to the world frame) where r_1, r_2, \dots, r_n are depths from drone to targets.

Unscented Kalman Filter estimator. As the drone follows a prescribed trajectory, different bearing measurements for the position of the target are acquired, and these measurements are fused in a UKF framework. The nonlinearity in the azimuth and elevation

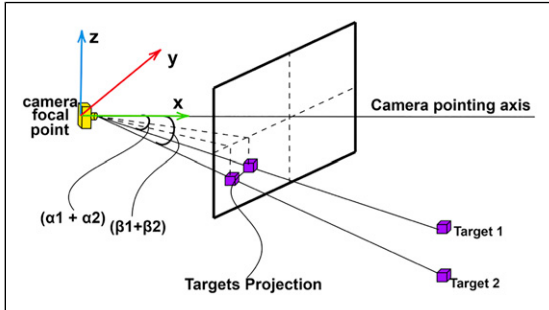


Figure 5. Image projection figure where $\alpha_1, \alpha_2, \beta_1$ and β_2 represent the bearing angles from the camera pointing axis to a vector that passes through the targets and the focal point.

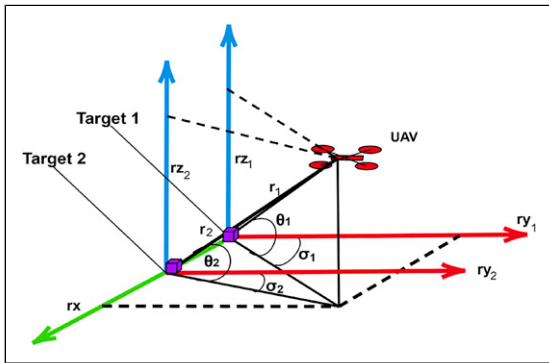


Figure 6. Obtained azimuth and elevation angles σ and θ for targets. r_1, r_2, \dots, r_n are depths from drone to targets expressed in r_x, r_y and r_z directions.

measurements (σ and θ) limits the performance of the standard linear Kalman filters even for stationary targets such as weeds. The UKF can perform better in encapsulating the nonlinear behaviour in the estimation process compared to the EKF, yet a better estimation is not always guaranteed. The following is the system's dynamics

$$\begin{aligned} X_{k+1} &= \Phi_{k+1,k} X_k + \lambda_k \\ Z_k &= h(X_k) + M_k \end{aligned} \quad (5)$$

Here, $X_k, X_{k+1} \in \mathbf{R}^3$ are the true target positions in ground fixed frame $X = [X^{(g)} \ Y^{(g)} \ Z^{(g)}]^T$ at time instants k and $k + 1$, respectively. The output $Z_k = [\sigma, \theta]^T \in [0, 2\pi] \times [0, \pi/2]$ is the bearing angle at time k . $h(X_k)$ is defined in (8). $\Phi_{k+1,k}$ is the state transition matrix of the system from the time k to $k + 1$. λ_k and M_k are the process and measurement noise, respectively, which are uncorrelated to Gaussian white noises with zero means and covariances μ_k and ψ_k , respectively, that is, ($\lambda \sim \mathcal{N}(0, \mu_k)$ and $M_k \sim \mathcal{N}(0, \psi_k)$). The process model is a 3×3 identity matrix since the targets are stationary; therefore, the process noise is a zero matrix

$$\phi_{k,k-1} = \begin{bmatrix} 1 & 0 & 0 \\ 0 & 1 & 0 \\ 0 & 0 & 1 \end{bmatrix}, \mu_k = \begin{bmatrix} 0 & 0 & 0 \\ 0 & 0 & 0 \\ 0 & 0 & 0 \end{bmatrix} \quad (6)$$

The measurement covariance matrix is

$$\psi_k = \begin{bmatrix} \sigma_1^2 & 0 \\ 0 & \sigma_1^2 \end{bmatrix} \quad (7)$$

From Figure 7, we can deduce that $r_{nx} = a_x - b_{nx}, r_{ny} = a_y - b_{ny}$ and $r_{nz} = a_z - b_{nz}$. Also, $a_k = [a_x \ a_y \ a_z]^T$ is the position of the UAV, $b_{nk} = [b_{nx} \ b_{ny} \ b_{nz}]^T$ are the targets positions and $r_{nk} = [r_{nx} \ r_{ny} \ r_{nz}]^T$ are the relative vectors between the UAV and target.

The measurement model is based on the azimuth angle σ and the elevation θ which are given for target n as follows

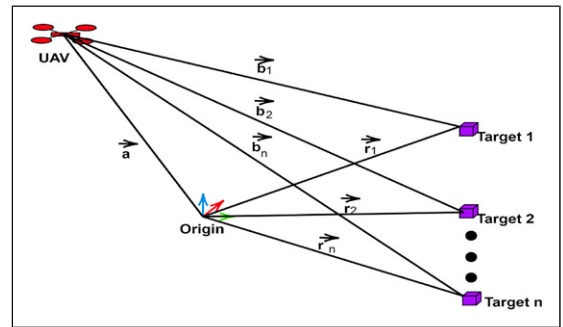


Figure 7. Vector representations of UAV's and targets positions.

$$Z_{nk} = \begin{bmatrix} \sigma_n \\ \theta_n \end{bmatrix} = \begin{bmatrix} \tan^{-1} \left(\frac{r_{nx}}{r_{ny}} \right) \\ \tan^{-1} \left(\frac{r_{nz}}{\sqrt{(r_{nx})^2 + (r_{ny})^2}} \right) \end{bmatrix} \quad (8)$$

The UKF model constitutes of firstly the time update step then the measurement update step. The time update encompasses the weight and the sigma points calculations. The measurement update utilizes the sigma points to generate covariance matrices and the Kalman gain.¹⁸

The time update. This process includes calculation of the sigma points and their weights and finally obtaining the time update equations after the Cholesky decomposition. We define the weights as

$$W_1 = \frac{\zeta}{n + \zeta} \quad (9)$$

$$W_i = \frac{1}{2(n + \zeta)}$$

where $i = 1, 2, \dots, n$ and n is the state vector dimension which is 3, and ζ is an arbitrary constant assigned to be 0. The sigma points at time k can be calculated as

$$\begin{aligned} S_{k-1} &= chol((n + \zeta)P_{k-1}) \\ X_{(0)} &= \hat{x}_{k-1} \\ X_{(i)} &= \hat{x}_{k-1} + S_{k-1}^{(i)} \end{aligned} \quad (10)$$

Similarly

$$\begin{aligned} X_{(i+n)} &= \hat{x}_{k-1} - S_{k-1}^{(i)} \\ X_{k-1} &= [X_{(0)} X_{(1)} \dots X_{(2n)}] \end{aligned} \quad (11)$$

where $i = 1, 2, \dots, n$. $S^{(i)}$ is the i th row vector of S and $chol$ means the Cholesky decomposition. Finally, the time update equations will be

$$\begin{aligned} \hat{X}_{\bar{k}} &= \sum_{i=0}^{2n} W_i f(X_i) \\ P_{\bar{k}} &= \sum_{i=0}^{2n} W_i \{f(X_i) - \hat{X}_{\bar{k}}\} \{f(X_i) - \hat{X}_{\bar{k}}\}^T + \mu_k \end{aligned} \quad (12)$$

Measurement update. The augmented sigma points can be obtained as

$$\begin{aligned} S_{\bar{k}} &= chol((n + \zeta)P_{k-1}) \\ X_{(0)} &= \hat{x}_{\bar{k}} \\ X_{(i)} &= \hat{x}_{\bar{k}} + S_{\bar{k}}^{(i)} \end{aligned} \quad (13)$$

Similarly

$$\begin{aligned} X_{(i+n)} &= \hat{x}_{\bar{k}} - S_{\bar{k}}^{(i)} \\ X_{\bar{k}} &= [X_{(0)} X_{(1)} \dots X_{(2n)}] \end{aligned} \quad (14)$$

where $i = 1, 2, \dots, n$.

$$\hat{z}_{\bar{k}} = \sum_{i=0}^{2n} W_i h(X_i) \quad (15)$$

Finally, the measurement covariance and the Kalman gain are calculated as

$$\begin{aligned} P_z &= \sum_{i=0}^{2n} W_i \{h(X_i) - \hat{z}_{\bar{k}}\} \{h(X_i) - \hat{z}_{\bar{k}}\}^T + \psi_k \\ G_k &= P_{xz} P_z^{-1} \end{aligned} \quad (16)$$

The final estimated state and it's covariance are

$$\begin{aligned} \hat{X}_k &= \hat{X}_{\bar{k}} + G_k (z_k - \hat{z}_{\bar{k}}) \\ P_k &= P_{\bar{k}} - G_k P_z G_k^T \end{aligned} \quad (17)$$

The position of the targets in ground frame is the output from the estimator.

Gazebo simulation and experimental set-up

Gazebo simulation set-up

For the simulation level verification experiments, the Gazebo environment is used in this paper. A model of the

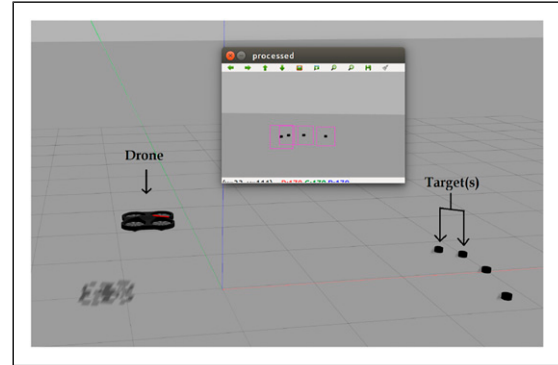


Figure 8. Gazebo environment set-up showing the drone and the targets.



Figure 9. Optitrack tracking camera.

Parrot AR drone was developed in Gazebo,³⁹ as demonstrated in Figure 8. The drone is equipped with all the sensors (monocular camera, rotors, ultrasonic sensors, etc.) as in the real platform. The properties of the sensors are assigned to match with real characteristics as best as possible.

For the simulation works, the ROS is used together with Gazebo. In addition to drone and sensors model, the ROS nodes responsible for the detection and classification of the weed using a DNN, centre pixel extraction on the images, calculating the bearing angles, fusing the bearing angles to estimate world coordinates of the weed with UKF and the trajectory planning and drone driving behavior



Figure 10. Parrot AR drone.

as the same in the real-time. A typical scene in Gazebo is presented in Figure 8. The black dot-like object represents the target/weed.

Experimental set-up

The experimental set-up includes Optitracks tracking system (see Figure 9), the Parrot drone (see Figure 10), the ground station and the target/weed. An indoor scene was created where real weeds were placed at some known positions. The Optitrack system is used to track the drone and also to obtain the ground truth positions of the targets. An actual Parrot drone shown in Figure 10 is subjected to a trajectory while the on-board monocular camera is utilized to detect these weeds. The trajectory parameters are selected such that the targets are covered in the FOV of the drone. A typical trajectory for four targets is seen in Figure 11 using a major axis radius $a = 0.6$ m and minor axis radius $b = 0.4$ m with a height of 1 m.

The centre pixels of the detected weeds are processed on the ground station to estimate the relative positions of the weeds. The weights of the fused-YOLO were exported as a static library with a function format which makes it easy to be called from any script. The MKLDNN libraries were linked so that neural network can run on the ground station CPU.⁴⁰

It is impossible to connect the workstation to the drone and the Optitracks at the same time. To overcome this issue, the internal configuration of the AR drone is updated so that it serves as a client and can be connected to a local network as shown in Figure 12.

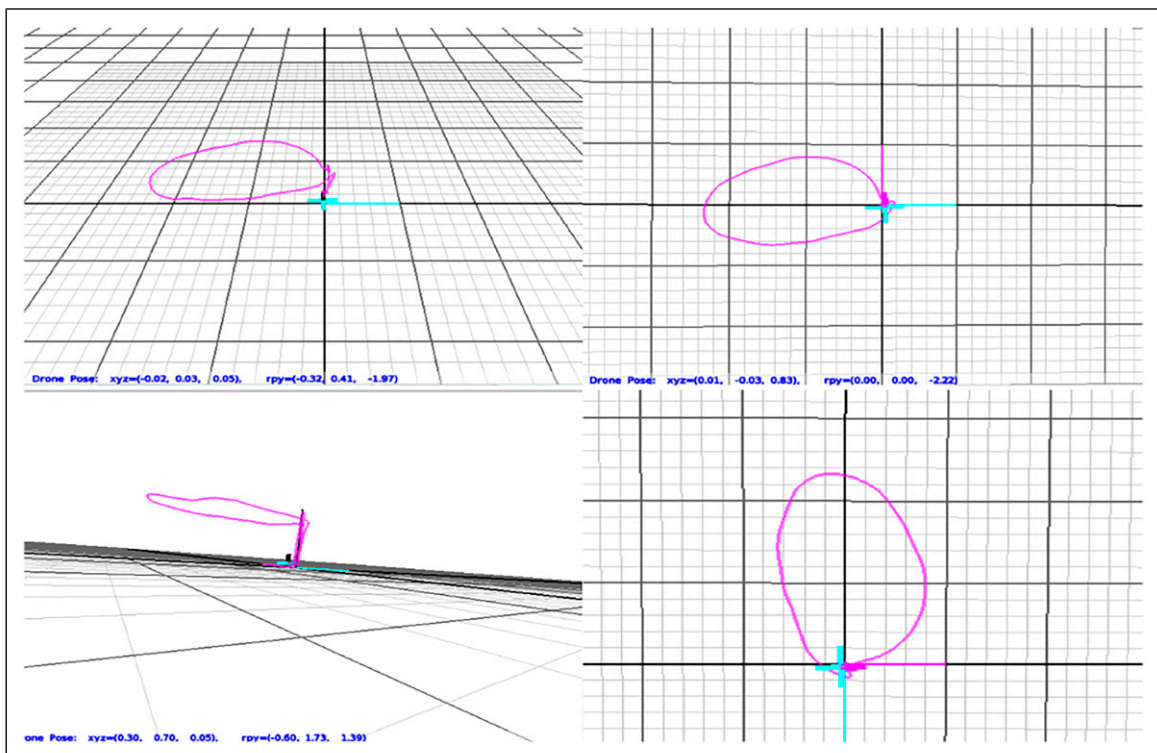


Figure 11. Obtained trajectory using a major axis radius = 0.6 m and minor axis radius = 0.4 m.

Connecting to the Optitracks is not enough to establish a pipeline to receive position updates, a supporting package is used to receive the broadcasted positions from the Optitracks so it can be used as a ROS topic and can be subscribed by any node. The real-time experiment was carried out on i7 Core CPU. It took approximately 45 seconds to complete the estimation which includes weed detection and localization as well. All the CPU cores were utilized with an average utilization factor of 90% while running the fused-YOLO. The frequency of the CPU was maintained at 2435 MHz.

Results

For both simulation and experimental works, the initialization was done arbitrarily; however, the initial state estimate and its covariance are taken as follows

$$\hat{X}_0 = \begin{bmatrix} 20 \\ 20 \\ 20 \end{bmatrix}, P_0 = \begin{bmatrix} 45 & 0 & 0 \\ 0 & 45 & 0 \\ 0 & 0 & 45 \end{bmatrix}, \zeta = 0 \quad (18)$$

Targets/weeds are placed at different ground truth positions. The drone is placed at $[x,y] = [0.00, 0.00] m$ for

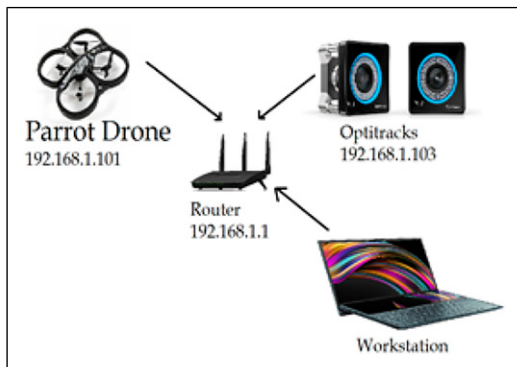


Figure 12. Network connection set-up.

simulations and experiments. For the simulations, the ground truth is obtained from the Gazebo simulation environment. For the experiments, both drone and targets are placed within the volume of the tracking system so that feedback of the ground truth positions can be received. The drone makes a trajectory within the volume while estimating the relative position of the placed targets. The ground truth of the experiment is different from the simulation to accommodate the tracking range of the Optitrack system. This will not have any effect on the estimation but in fact proves the robustness of the estimation at different ground truth positions.

Simulation results

The simulation results were analyzed by comparing the estimated positions with the ground truth position. Weeds were placed at ground truth positions $[x, y] = [4.00, 1.00], [3.50, 0.50], [3.00, 0.00], [2.50, -0.50] m$. For the longitudinal tests, we estimate the x component of the ground truth, that is, $[x] = [4.00], [3.50], [3.00], [2.50] m$. In Figure 13, the dashed lines represent the ground truth position while the continuous lines represent the estimated position. The results show the convergence of the estimator along x-axis of the ground frame: the estimated positions were obtained after 35 seconds of estimation process which is decent compared to the literature.^{18,34} Figure 13 also shows the changes in the estimation error with time. The error is measured as the absolute difference between the ground truth position and the estimated position. The error approaches to zero as the estimator receives updates.

The 2D localization of the weed is performed simultaneously. For the lateral tests, we estimate the y component of the ground truth, that is, $[y] = [1.00], [0.50], [0.00], [-0.50] m$. The results are demonstrated in Figure 14. The performance of the proposed solution along the lateral axis is satisfactory and gets better through time, as expected.

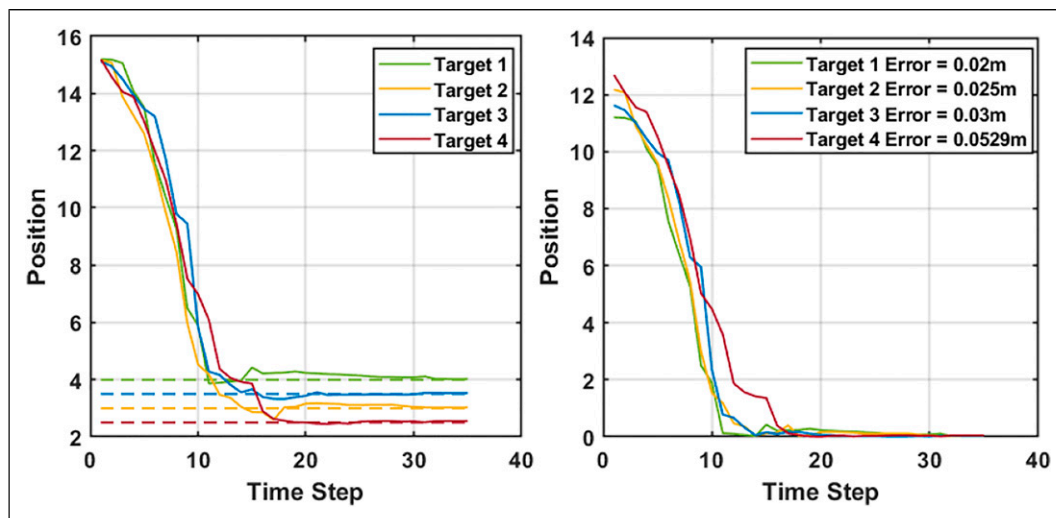


Figure 13. Coordinate estimation and error (simulation tests along x-axis). The dashed lines represent the ground truth while the continuous lines are the estimations.

To further verify the robustness of the estimator, the same experiment was conducted with different ground truth position. Table 1 presents the experiment scenario and the results. The results prove the success of the position estimation with no sophisticated sensors in the simulation environment. An average error of 0.066 m was obtained along the x direction and 0.082 m along the y direction.

Experimental results

Detection score. The accuracy of detection has an effect on the overall estimation performance, since the centre of bounding box of the detected weeds is assumed to match the geometric centres of the targets. The detection score evaluates how well a bounding box is assigned to a target $C_b = C_t$, where C_b and C_t are the centres of bounding box and target, respectively, so that the bounding box

accurately covers the area of the target. The lowest detection score recorded for all the targets/weeds detected is 79% and the maximum is 95%. Figure 15 shows the detection scores with their frequencies. The frequency in this context is defined as how many times a particular detection score was obtained throughout the estimation.

Detection deviation. The detection deviation is defined to indicate how much is the deviation in $C_b \neq C_t$. It provides a clear indication about the error that is introduced to the estimator due to misleading extraction of the centre position of the bounding box. It is defined as the difference between the ideal detection score and the obtained detection score. For the experimental works, the deviation score is limited to 21%, which means that up to 21% deviation in C_b from C_t is considered tolerable for obtaining an accurate estimation. The histogram plot for the deviation is shown in Figure 16.

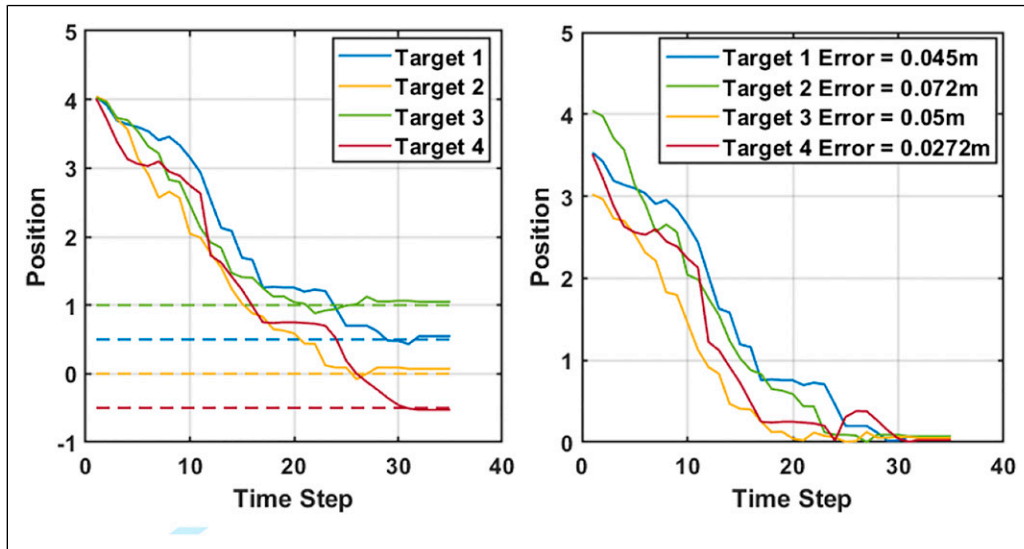


Figure 14. Coordinate estimation and error (simulation tests along y -axis). The dashed lines represent the ground truth while the continuous lines are the estimations.

Table 1. Additional simulation results using YOLOv4 with targets placed at positions $[x, y] = [4.00, 0.22]$, $[3.00, 0.036]$, $[3.00, 0.50]$, $[3.50, -0.36]$ and $[2.80, -0.06]$. The error of estimation is the difference between the ground truth and the estimated positions.

Takes	Ground truth (x)	Estimated (x)	Error (x)
1	4.00	3.85	0.15
2	3.00	3.10	0.10
3	3.00	3.03	0.03
4	3.50	3.47	0.03
5	2.80	2.82	0.02
Takes	Ground truth (y)	Estimated (y)	Error (y)
1	0.22	0.127	0.093
2	0.036	0.025	0.011
3	0.50	0.610	0.11
4	-0.36	-0.51	0.15
5	-0.06	-0.016	0.044

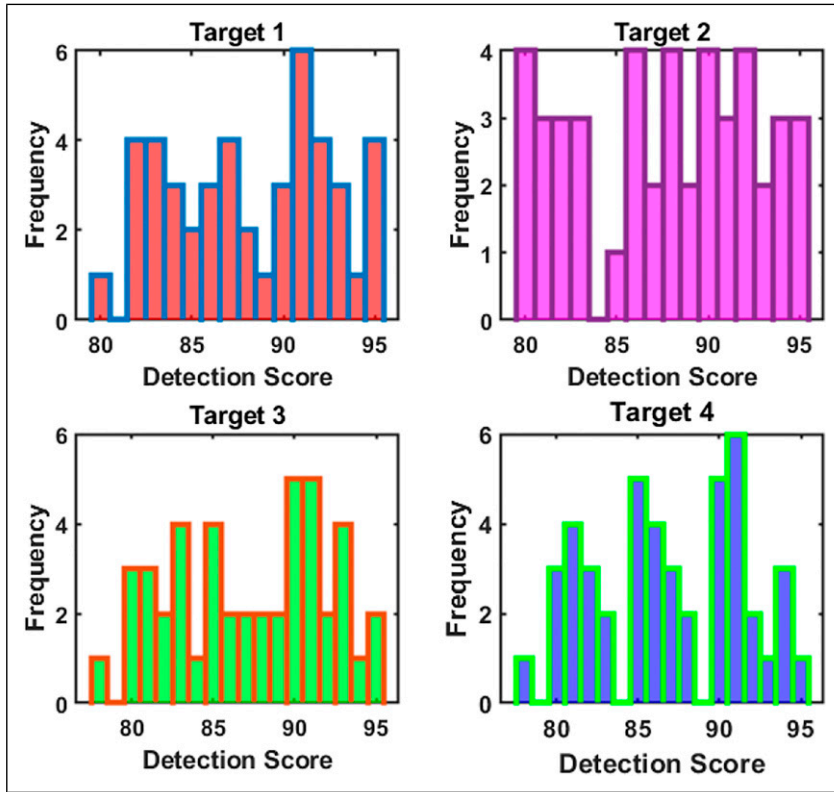


Figure 15. Detection score.

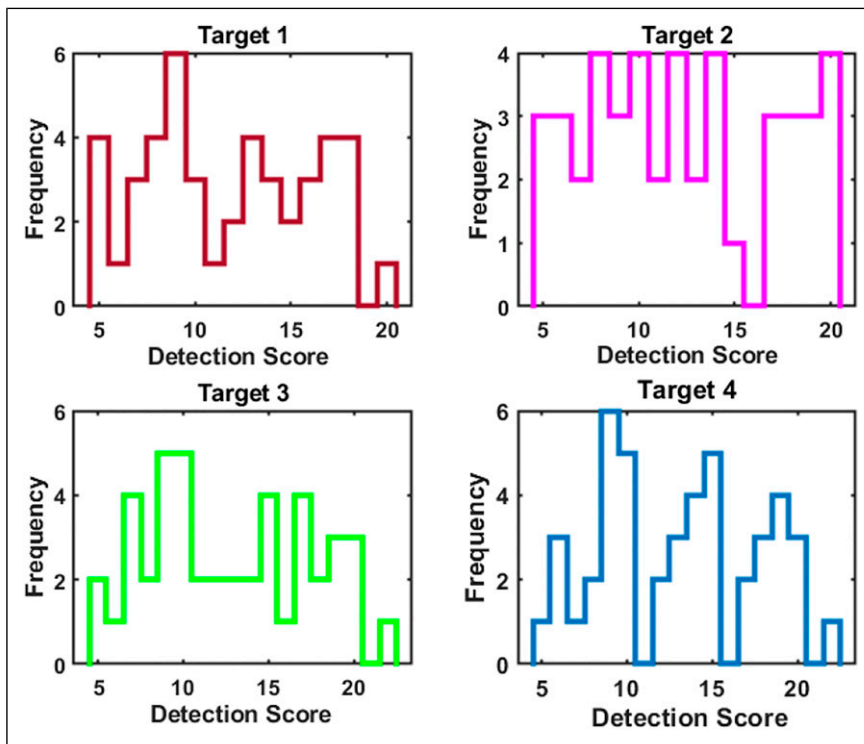


Figure 16. Detection deviation.

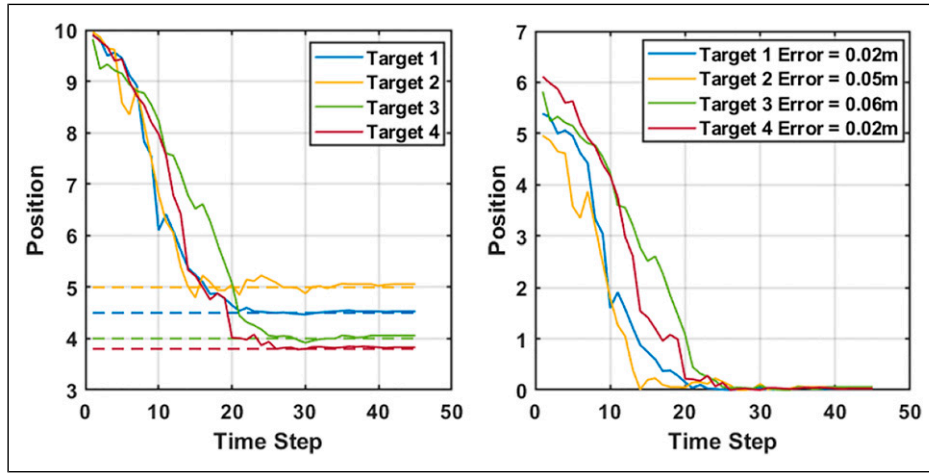


Figure 17. Coordinate estimation and error (experimental tests along x-axis). The dashed lines represent the ground truth while the continuous lines are the estimations.

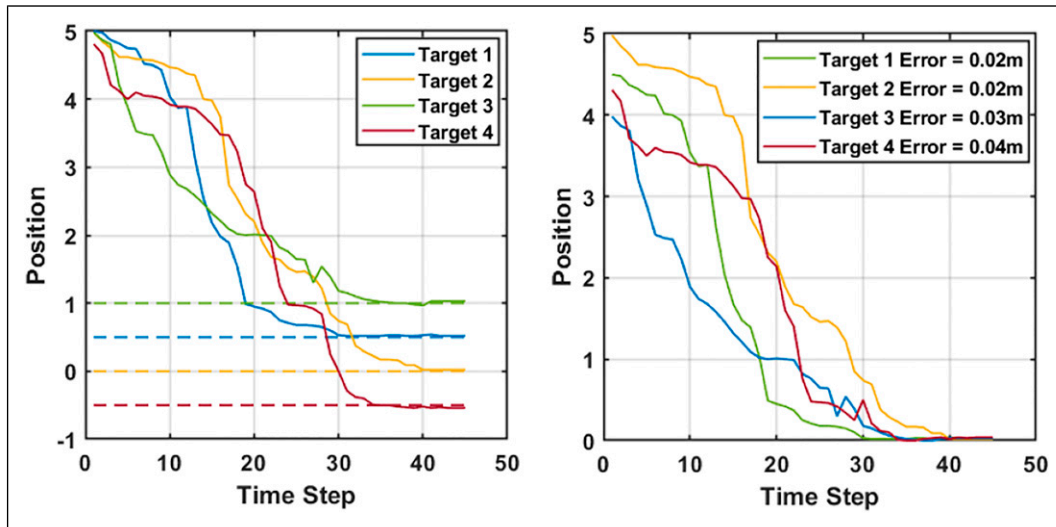


Figure 18. Coordinate estimation and error (experimental tests along y-axis). The dashed lines represent the ground truth while the continuous lines are the estimations.

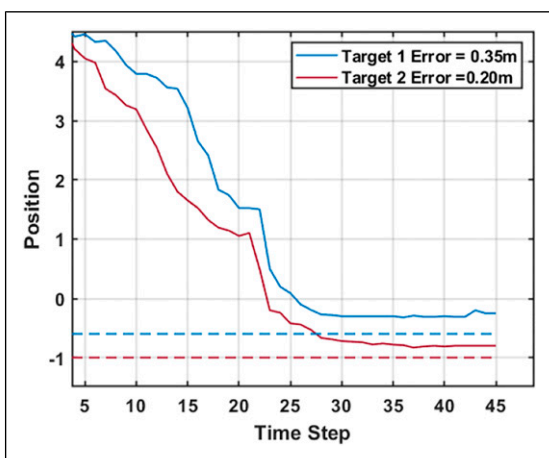


Figure 19. Coordinate estimation and error (experimental tests along y-axis, insufficient Optitrack data case). The dashed lines represent the ground truth while the continuous lines are the estimations.

Position estimation. As the drone follows its predefined elliptical trajectory, the depth, the azimuth and elevation angles vary continuously, and the measurements are fused to estimate the positions of targets. Weeds were placed at ground truth positions $[x, y] = [5.00, 1.00], [4.50, 0.50], [4.00, 0.00], [3.80, -0.50] m$. For the longitudinal tests, we estimate the x component of the position as $[x] = [5.00], [4.50], [4.00], [3.80] m$. The estimated positions and the position estimation errors are shown in [Figure 17](#). For the lateral tests, the y component of the position is estimated, and the results are demonstrated in [Figure 18](#).

To show the robustness of the proposed scheme, a test is conducted where the Optitrack cannot sufficiently provide feedback to the drone for control. The fixed altitude assumption is violated in these experiments, and consequently, the estimator recorded a greater error in these scenarios, as can be seen in [Figure 19](#). Targets were placed at a y coordinate $[y] = [-0.60], [-1.00]m$, and the drone was placed at initial position $[x, y] = [-1.00, 0.00] m$

Table 2. Additional experimental results using YOLOv4 with targets placed at positions $[x, y] = [4.62, 0.00], [4.43, 0.50], [5.12, -0.50], [3.89, 1.00]$ and $[4.04, -1.00]$. The error of estimation is the difference between the ground truth and the estimated positions.

Takes	Ground truth (x)	Estimated (x)	Error (x)
1	4.62	4.57	0.03
2	4.43	4.45	0.03
3	5.12	5.19	0.07
4	3.89	3.77	0.10
5	4.04	4.09	0.05

Takes	Ground truth (y)	Estimated (y)	Error (y)
1	0.00	0.05	0.05
2	0.50	0.49	0.01
3	-0.50	-0.26	0.24
4	1.00	1.065	0.065
5	-1.00	-1.20	0.20

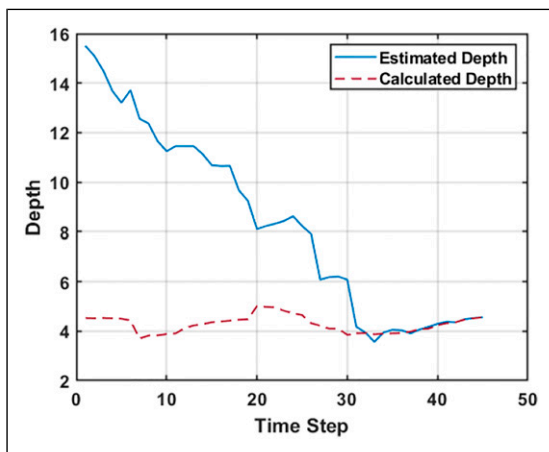


Figure 20. Depth estimation.

such that not all updates will be received because of a limited tracking volume. In other words, the drone cannot be tracked at some points along the trajectory. Despite this disturbance, a maximum error of 0.35 m was experienced.

More experimental results were obtained repeating the same experiment with different ground truth positions to verify the robustness. Table 2 shows the obtained estimation with the associated error. An average error of 0.056 m was obtained along the x direction and 0.113 m along the y direction.

Depth estimation. The depth, r , estimation from the UKF is compared with the depth measured using the positions of the UAV and the target obtained with the Optitrack system. Since the UAV's height H is known, the depth will be equal to $\sqrt{(D)^2 + (H)^2}$, where D is the difference of the target's position and the UAV's position along the direction of the camera frame. Flying at a fixed height of 1 m will reduce the depth to

$\sqrt{(D)^2 + 1}$. Figure 20 shows the convergence of the estimated depth and the calculated depth. The calculated depth is not constant as the drone is subjected to an elliptical trajectory; thus, a varying elevation angle θ will be received along the trajectory. It is observed that with time, the depth estimation gets better and resembles the acceptable level.

The experimental results converge after 45 seconds while the simulation results converge after 35 seconds. This is majorly due to the latency as the image updates are transported over a network in the experimental set-up. On the other hand, the simulation set-up assumes an ideal world with no update delay.

Detection score comparison. Our pipeline can be utilized with different YOLO versions by simply substituting the detection end of the pipeline. This shows how flexible the pipeline proposed is since it can easily be adapted to other versions of YOLO. This can be done by truncating the final layers of ResNet-50 and utilizing the final activation layer of the ResNet as the feature extraction of the preferred YOLO version as earlier explained in Figure 2. Provided a detection is made and a bounding box is assigned to the target, detected target's position can be estimated. However, there can be a slight deviation in detection score across different YOLO versions.

Newer versions of YOLO such as YOLOv4 may have better accuracy and FPS. However, these properties may not significantly increase the overall accuracy of the estimation since the detection is performed at regular time steps. Nonetheless, the most sensitive parameter is the detection score which can introduce error to the estimation. A better detection score will result in a better estimation. We define the detection score as how well the centre of the bounding box aligns with the centre pixels of the target. We have compared the detection scores obtained using both YOLOv2⁴¹ and YOLOv4 as the final layers of the proposed architecture across 45 time steps for each target as seen in

Table 3. Additional experimental results comparing YOLOv2 (v2) and YOLOv4 (v4) estimations with targets placed at ground truth positions (GT) $[x, y] = [4.62, 0.00], [4.43, 0.50], [5.12, -0.50], [3.89, 1.00]$ and $[4.04, -1.00]$.

Takes	GT (x)	Estimated v2 (x)	Error v2 (x)	Estimated v4 (x)	Error v4 (x)
1	4.62	4.58	0.04	4.57	0.03
2	4.43	4.45	0.03	4.45	0.03
3	5.12	5.21	0.09	5.19	0.07
4	3.89	3.78	0.11	3.77	0.10
5	4.04	4.09	0.05	4.09	0.05

Takes	GT (y)	Estimated v2 (y)	Error v2 (y)	Estimated v4 (y)	Error v4 (y)
1	0.00	0.06	0.06	0.05	0.05
2	0.50	0.49	0.01	0.49	0.01
3	-0.50	-0.23	0.27	-0.26	0.24
4	1.00	1.07	0.07	1.065	0.065
5	-1.00	-1.20	0.20	-1.20	0.20

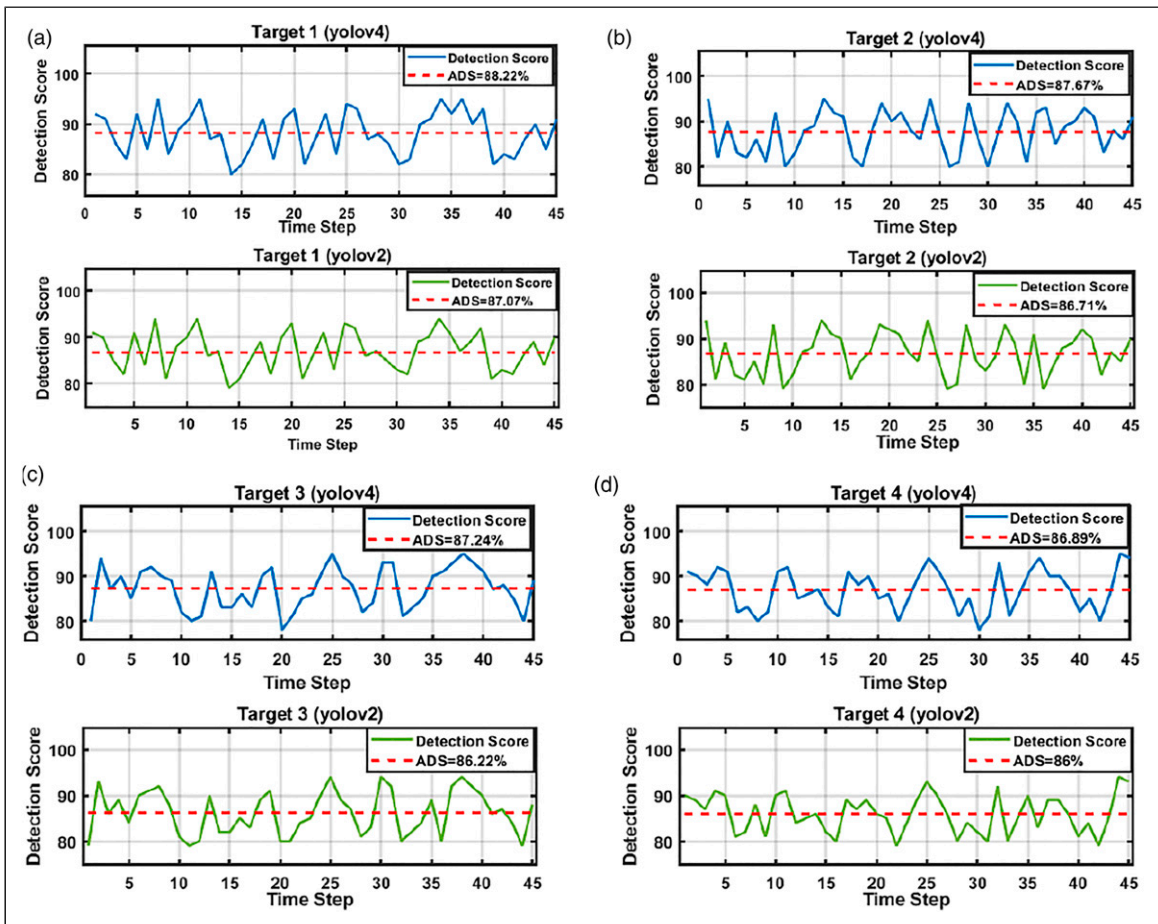


Figure 21. (a) Detection score comparison between YOLOv2 and YOLOv4 for target 1, (b) detection score comparison between YOLOv2 and YOLOv4 for target 2, (c) detection score comparison between YOLOv2 and YOLOv4 for target 3 and (d) detection score comparison between YOLOv2 and YOLOv4 for target 4.

Figure 21. The overall average detection score (ADS) for the four targets using YOLOv4 is 87.505% while with YOLOv2 it is 86.5%. Although both ADS fall within an acceptable range for this experiment, YOLOv4 is expected

to provide a slightly more accurate result than YOLOv2 since it has a better detection score.

Table 3 compares the estimation of target positions performed using both YOLOv2 and YOLOv4 as

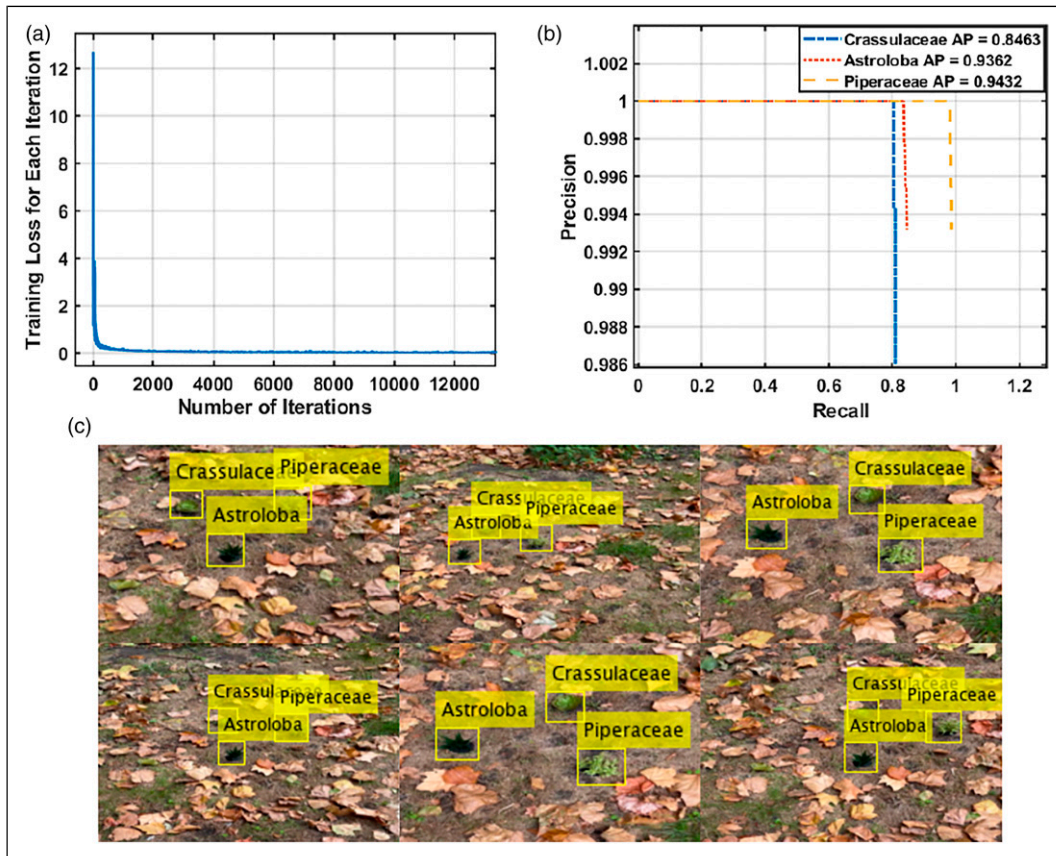


Figure 22. (a) Training loss per iteration for fused-YOLO network in an indoor setting, (b) precision/recall results for *Crassulaceae*, *Astroloba* and *Piperaceae* with their respective AP in an indoor setting and (c) qualitative result samples from fused-YOLO network in an indoor setting.

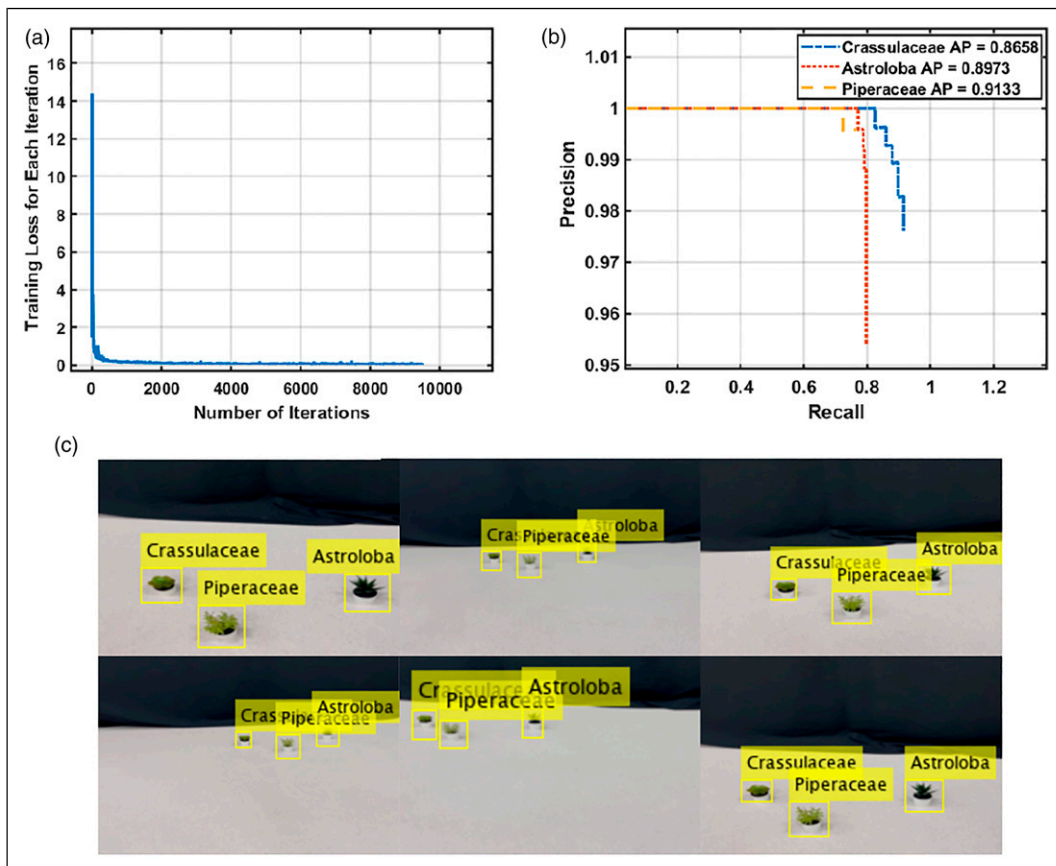


Figure 23. (a) Training loss per iteration for fused-YOLO network in an outdoor setting, (b) precision/recall results for *Crassulaceae*, *Astroloba* and *Piperaceae* with their respective AP in an outdoor setting and (c) qualitative result samples from Fused-YOLO network in an outdoor setting.

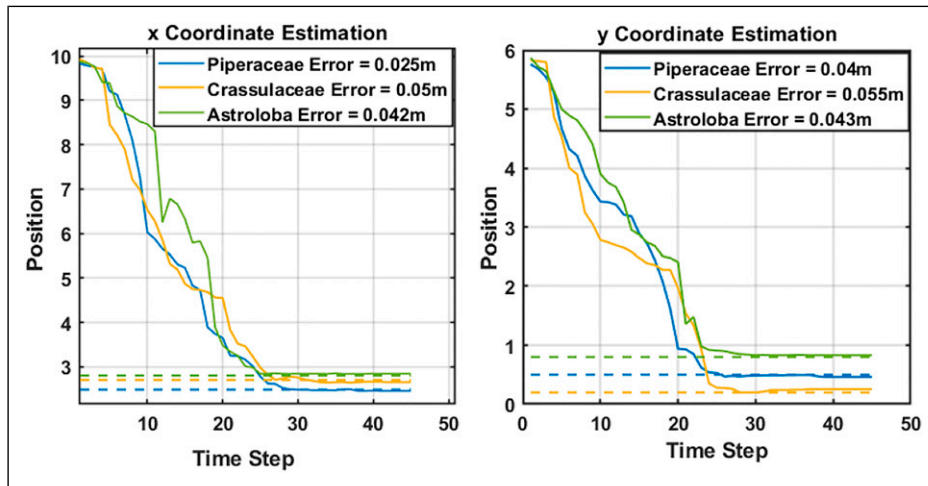


Figure 24. Coordinate estimation $[x, y]$ (experimental tests with different classes of weeds). The dashed lines represent the ground truth while the continuous lines are the estimations.

detectors. Targets were placed at ground truth positions $[x, y] = [4.62, 0.00]$, $[4.43, 0.50]$, $[5.12, -0.50]$, $[3.89, 1.00]$ and $[4.04, -1.00]$ while estimation was performed over 45 time steps. The average estimation error using YOLOv2 is $[x, y] = [0.064 \text{ m}, 0.122 \text{ m}]$ while YOLOv4 performed slightly better at $[x, y] = [0.056 \text{ m}, 0.113 \text{ m}]$ due to a slightly better detection score.

Network performance. We validated the performance of the proposed network both in the indoor and the outdoor scenarios. Three classes of weeds, namely, *Crassulaceae*, *Astroloba* and *Piperaceae* are used in the experiments. The obtained final training loss was 0.032 for the outdoor training as seen in Figure 22(a). The outdoor validation in Figure 22(b) shows the Average Precision (AP) obtained for these weed classes. *Crassulaceae* obtained an AP of 0.8643, *Astroloba* obtained an AP of 0.9362 and *Piperaceae* obtained an AP of 0.9432 across 443 frames. Samples of the detection using the fused-YOLO network are displayed in Figure 22(c). The bounding boxes as seen in most cases are corresponding to the target's centre which will facilitate better position estimation. For the indoor setting, a final training loss of 0.0203 was obtained as shown in Figure 23(a). The validation results from Figure 23(b) show the AP of *Crassulaceae* class at 0.8658, *Astroloba* at 0.8973, while *Piperaceae* obtained an AP of 0.9133 evaluated across 315 frames.

Another experiment was conducted to estimate the positions of the different classes of weeds concurrently. The different classes of weeds (*Crassulaceae*, *Astroloba* and *Piperaceae*) were placed at ground truth positions at $[x, y] = [2.7, 0.2]$, $[2.8, 0.8]$ and $[2.48, 0.5]$, respectively. The error obtained for each class is shown in Figure 24. An error of $[x, y] = [0.05 \text{ m}, 0.055 \text{ m}]$ was observed for *Crassulaceae* class while for *Piperaceae* and *Astroloba* classes, the errors are found to be $[x, y] = [0.025 \text{ m}, 0.04 \text{ m}]$ and

$[x, y] = [0.042 \text{ m}, 0.043 \text{ m}]$, respectively. These results further validate that the proposed pipeline can effectively estimate the positions of different classes (types) of weeds.

Conclusion

This paper shows the implementation of relative position estimation for multiple targets (weeds) by the combination of UKF with a deep neural network. It addresses the use of sophisticated algorithms for position estimation and detection of weeds, and presented a faster and reliable accuracy using affordable sensors. It extends to not only using bounding boxes for detection but utilizing them for position estimation.

In the proposed solution for weed detection, an affordable UAV platform with a monocular camera is used. Weeds are detected and classified using a trained neural network and the detection boxes are utilized to extract the centre of the target using the image data from the UAV platform which performs an elliptic trajectory and thus forms the basis for the varying bearing angles for UKF estimation. The UKF utilizes the noisy azimuth and elevation angles to perform the estimation.

The simulation results converge after 35 seconds while the experimental results converge after 45 seconds. The detection score was 87.5% in average. Overall average estimator error is $(x = 0.056 \text{ m}, y = 0.0703 \text{ m})$. The proposed method is able to achieve multiple target (weed) position estimation with lesser error margin using an off-the-shelf platform without requiring any sophisticated or additional devices or sensors. The estimation error is measured from the weed's centre, and most detectable weeds have a cross-section of up to or more than 10 cm. Also, these positions are estimated positions, and mechanical weeding arms or sprayers are usually accompanied with camera to perform visual servoing (post-processing) to fine tune the exact positions of the target, and hence, these results are satisfactory for this mission.

For the future works, this method can be extended to dynamically optimize the trajectory for the estimation for better field of view so more targets/weeds can be estimated. Cooperative estimation can be investigated for faster convergence.

Declaration of conflicting interests

The author(s) declared no potential conflicts of interest with respect to the research, authorship, and/or publication of this article.

Funding

The author(s) received no financial support for the research, authorship, and/or publication of this article.

ORCID iDs

Mahmoud Abdulsalam  <https://orcid.org/0000-0002-6546-2340>

Kenan Ahiska  <https://orcid.org/0000-0002-7215-6675>

References

1. Pusphavalli M and Chandraleka R. Automatic weed removal system using machine vision. *JARECE* 2016; 5(3): 503–506.
2. Altieri MA, Van Schoonhoven A and Doll J. The ecological role of weeds in insect pest management systems: a review illustrated by bean (*phaseolus vulgaris*) cropping systems. *Pans* 1977; 23(2): 195–205.
3. Lanini W, Strange M, et al. Low-input management of weeds in vegetable fields. *Calif Agric* 1991; 45(1): 11–13.
4. Hodgson JM. *The nature, ecology, and control of Canada thistle. 1386, agricultural research service*. Washington DC, United States of America: US Department of Agriculture, 1968.
5. Monaco T, Grayson A and Sanders D. Influence of four weed species on the growth, yield, and quality of direct-seeded tomatoes (*lycopersicon esculentum*). *Weed Sci* 1981; 29(4): 394–397.
6. Bakker T, van Asselt K, Bontsema J, et al. An autonomous weeding robot for organic farming. In: *Field and service robotics*. Berlin, Germany: Springer, pp. 579–590.
7. Tang JL, Chen XQ, Miao RH, et al. Weed detection using image processing under different illumination for site-specific areas spraying. *Comput Electron Agric* 2016; 122: 103–111.
8. Gonzalez-de Soto M, Emmi L, Perez-Ruiz M, et al. Autonomous systems for precise spraying—evaluation of a robotised patch sprayer. *Biosyst Eng* 2016; 146: 165–182.
9. Malneršič A, Dular M, Širok B, et al. Close-range air-assisted precision spot-spraying for robotic applications: aerodynamics and spray coverage analysis. *Biosyst Eng* 2016; 146: 216–226.
10. Oberti R, Marchi M, Tirelli P, et al. Selective spraying of grapevines for disease control using a modular agricultural robot. *Biosyst Eng* 2016; 146: 203–215.
11. Herrera PJ, Dorado J and Ribeiro Á. A novel approach for weed type classification based on shape descriptors and a fuzzy decision-making method. *Sensors* 2014; 14(8): 15304–15324.
12. Zheng YY, Kong JL, Jin XB, et al. Cropdeep: the crop vision dataset for deep-learning-based classification and detection in precision agriculture. *Sensors* 2019; 19(5): 1058.
13. Lottes P, Khanna R, Pfeifer J, et al. UAV-based crop and weed classification for smart farming. In: Proceedings of the IEEE International Conference on Robotics and Automation (ICRA), Singapore, May 2017. IEEE, pp. 3024–3031.
14. Yu J, Schumann AW, Cao Z, et al. Weed detection in perennial ryegrass with deep learning convolutional neural network. *Front Plant Sci* 2019; 10: 1422.
15. Quigley M, Conley K, Gerkey B, et al. ROS: an open-source robot operating system. In: Proceedings of the ICRA Workshop on Open Source Software: Volume 3, Kobe, Japan, January 2009, p. 5.
16. Guimarães RL, de Oliveira AS, Fabro JA, et al. Ros navigation: concepts and tutorial. In: *Robot operating system (ROS)*. Berlin, Germany: Springer, 2016, pp. 121–160.
17. Marin-Plaza P, Hussein A, Martin D, et al. Global and local path planning study in a ros-based research platform for autonomous vehicles. *J Adv Transp* 2018; 2018: 1–10.
18. Dena Ruiz J and Aouf N. Unscented Kalman filter for vision based target localisation with a quadrotor. *ICINCO* 2017; 2: 453–458.
19. He K, Zhang X, Ren S, et al. Deep residual learning for image recognition. In: Proceedings of the IEEE Conference on Computer Vision and Pattern Recognition, Las Vegas, NV, USA, December 2016, pp. 770–778.
20. Bochkovskiy A, Wang CY and Liao HYM. Yolov4: optimal speed and accuracy of object detection. 2020. arXiv preprint arXiv: 200410934 2020.
21. Wan EA and Van Der Merwe R. The unscented Kalman filter for nonlinear estimation. In: Proceedings of the IEEE 2000 Adaptive Systems for Signal Processing, Communications, and Control Symposium (Cat. IEEE: No. 00EX373), Lake Louise, AB, Canada, October 2000, pp. 153–158.
22. Gomez-Balderas JE, Flores G, Carrillo LG, et al. Tracking a ground moving target with a quadrotor using switching control. *J Intell Robot Syst* 2013; 70(1): 65–78.
23. Paikerkari A, Ghule V, Meshram R, et al. Weed detection using image processing. *IRJET* 2016; 3(3): 1220–1222.
24. Islam N, Rashid MM, Wibowo S, et al. Early weed detection using image processing and machine learning techniques in an australian chilli farm. *Agriculture* 2021; 11(5): 387.
25. Simonyan K and Zisserman A. Very deep convolutional networks for large-scale image recognition. Proceedings of International Conference on Learning Representations, San Diego, California, 2014. arXiv preprint arXiv: 14091556 2014.
26. Lottes P, Behley J, Milioto A, et al. Fully convolutional networks with sequential information for robust crop and weed detection in precision farming. *IEEE Robot Autom Let* 2018; 3(4): 2870–2877.
27. Abdulsalam M and Aouf N. Deep weed detector/classifier network for precision agriculture. In: Proceedings of the 28th Mediterranean Conference on Control and Automation (MED). IEEE, Saint-Raphael, France, September 2020. pp. 1087–1092.
28. Liu B and Bruch R. Weed detection for selective spraying: a review. *Curr Robot Rep* 2020; 1(1): 19–26.
29. Wang A, Zhang W and Wei X. A review on weed detection using ground-based machine vision and image processing techniques. *Comput Electron Agric* 2019; 158: 226–240.
30. Hou Y and Yu C. Autonomous target localization using quadrotor. In: Proceedings of the 26th Chinese Control and Decision Conference (2014 CCDC), Changsha, China, May 2014, IEEE, pp. 864–869.
31. Redding JD, McLain TW, Beard RW, et al. Vision-based target localization from a fixed-wing miniature air vehicle.

- In: Proceedings of the American Control Conference, Minneapolis, MN, USA, June 2006, IEEE, p. 6.
32. Deneault D, Schinstock D and Lewis C. Tracking ground targets with measurements obtained from a single monocular camera mounted on an unmanned aerial vehicle. in Proceedings of the IEEE International Conference on Robotics and Automation, Pasadena, CA, USA, May 2008, IEEE, pp. 65–72.
 33. Hosseinpoor H, Samadzadegan F and Dadras Javan F. Precise target geolocation and tracking based on uav video imagery. *Int Arch Photogramm Remote Sens* 2016; 41: 243–249.
 34. Ponda S, Kolacinski R and Frazzoli E. Trajectory optimization for target localization using small unmanned aerial vehicles. In: Proceedings of the AIAA Guidance, Navigation, and Control Conference, Chicago, IL, USA, August 2009, p. 6015.
 35. *Developer guide SDK 2.0*, 2021. <https://jpchanson.github.io/ARdrone/ParrotDevGuide.pdf>
 36. *Motive: prime 13 - in depth*, 2021. <https://optitrack.com/cameras/primex-13/>
 37. Mueggler E, Faessler M, Fontana F, et al. Aerial-guided navigation of a ground robot among movable obstacles. In: Proceedings of the IEEE International Symposium on Safety, Security, and Rescue Robotics, Hokkaido, Japan, October 2014, IEEE, pp. 1–8.
 38. Jiang H, Zhang C, Qiao Y, et al. CNN feature based graph convolutional network for weed and crop recognition in smart farming. *Comput Electron Agric* 2020; 174: 105450.
 39. Engel J, Sturm J and Cremers D. Scale-aware navigation of a low-cost quadcopter with a monocular camera. *Rob Auton Syst* 2014; 62(11): 1646–1656.
 40. Zarukin D. *oneapi-src/onednn*, 2021. <https://github.com/oneapi-src/oneDNN>
 41. Redmon J, Divvala S, Girshick R, et al. You only look once: unified, real-time object detection. In: Proceedings of the IEEE Conference on Computer Vision and Pattern Recognition. Boston, MA, USA, June 2016, pp. 779–788.